ADVANCED OPTICAL MATERIALS
www.advopticalmat.de

A Multilayer-Based Visibly Transparent Radiative Cooler with Enhanced Solar Selectivity

Juhoon Baek, Minseo Jeong, Doyoon Lee, Huu Lam Phan, Dasol Lee,* and Minkyung Kim**

Transparent radiative cooling enables passive thermal management by selectively reflecting solar radiation and emitting thermal energy, thereby offering a promising solution for energy-efficient cooling in transparent applications. Despite recent progress in the development of transparent radiative coolers, achieving a balance between high visible transparency and effective solar reflection remains a critical challenge in enhancing the cooling performance. In this study, a transparent radiative cooler comprising a 50 µm-thick polydimethylsiloxane (PDMS) emitter integrated with a sophisticated metal-dielectric multilayer is evaluated both experimentally and theoretically. The theoretical simulations demonstrate a visible transmittance >82% and a near-infrared reflectance >92%, with a sharp transition between spectral regimes. Experimental characterizations confirm a visible transmittance of 48% alongside an enhanced near-infrared reflectance of 98%, thereby validating robust cooling performance under real-world conditions. Additionally, daytime outdoor measurements indicate that the cooler achieves a maximum temperature reduction of 10.8 °C compared to conventional PDMS-coated glass. Furthermore, global simulations illustrate the cooling effect of this cooler under diverse climatic conditions, highlighting its potential for use in various terrestrial areas.

1. Introduction

The accelerating pace of global warming has intensified the global energy demand, primarily propelled by our expanding reliance on cooling and refrigeration systems. These conventional and inherently energy-intensive cooling technologies contribute substantially to greenhouse gas emissions and further exacerbate climate change. To address this issue, radiative cooling, which requires no additional energy input, has gained significant attention.[1–5] Among the various radiative cooling technologies reported to date, visibly transparent radiative cooling has emerged as a promising solution for applications requiring both cooling and optical transparency. This approach offers the unique advantage of maintaining visible transparency while achieving cooling and has been developed for a wide range of applications,[6] such as building energy saving,[7,8] windows,[9,10] photovoltaic panels,[11] and electronic devices.[12]

A transparent radiative cooler typically consists of a mid-infrared (MIR) emitter and a near-infrared (NIR) reflector, each playing a crucial role in maximizing the cooling efficiency (**Figure 1a**). The emitter facilitates heat dissipation by radiating thermal energy from the object into space, particularly through the atmospheric window (8–13 µm) in the MIR range, where the blackbody radiation of a room-temperature body dominates. The emitter must exhibit high emissivity within the atmospheric window to achieve optimal radiative cooling. Meanwhile, the NIR reflective layer reduces the total energy input to the surface by reflecting solar radiation, with the exception of that falling within the visible spectrum (0.7–2.5 µm). The optical properties of the cooler must transition at ≈700 nm to ensure a high transmittance in the visible range for optical applications, while increasing reflectance in the nonvisible regime to enhance the radiative cooling performance. Since ≈44% of total solar irradiance is distributed within the visible spectrum (0.38–0.7 µm), blocking unwanted solar energy significantly improves the thermal efficiency of the cooler while maintaining visible transparency.

Despite the NIR reflection, the cooling capabilities of transparent radiative coolers are inevitably lower than those of conventional radiative coolers[13,14] due to solar absorption in the visible range.[15,16] As a result, enhancing their cooling

J. Baek, D. Lee, H. L. Phan, M. Kim
School of Mechanical and Robotics Engineering
Gwangju Institute of Science and Technology (GIST)
Gwangju 61005, Republic of Korea
E-mail: phanhuulam@gist.ac.kr; phlam@ntt.edu.vn; m.kim@gist.ac.kr

M. Jeong, D. Lee
Department of Biomedical Engineering
Yonsei University
Wonju 26493, Republic of Korea
E-mail: dasol@yonsei.ac.kr

H. L. Phan
Mechatronics and Robotics Research Group
Faculty of Engineering and Technology
Nguyen Tat Thanh University
Ho Chi Minh 700000, Vietnam

The ORCID identification number(s) for the author(s) of this article can be found under https://doi.org/10.1002/adom.202501509

DOI: 10.1002/adom.202501509

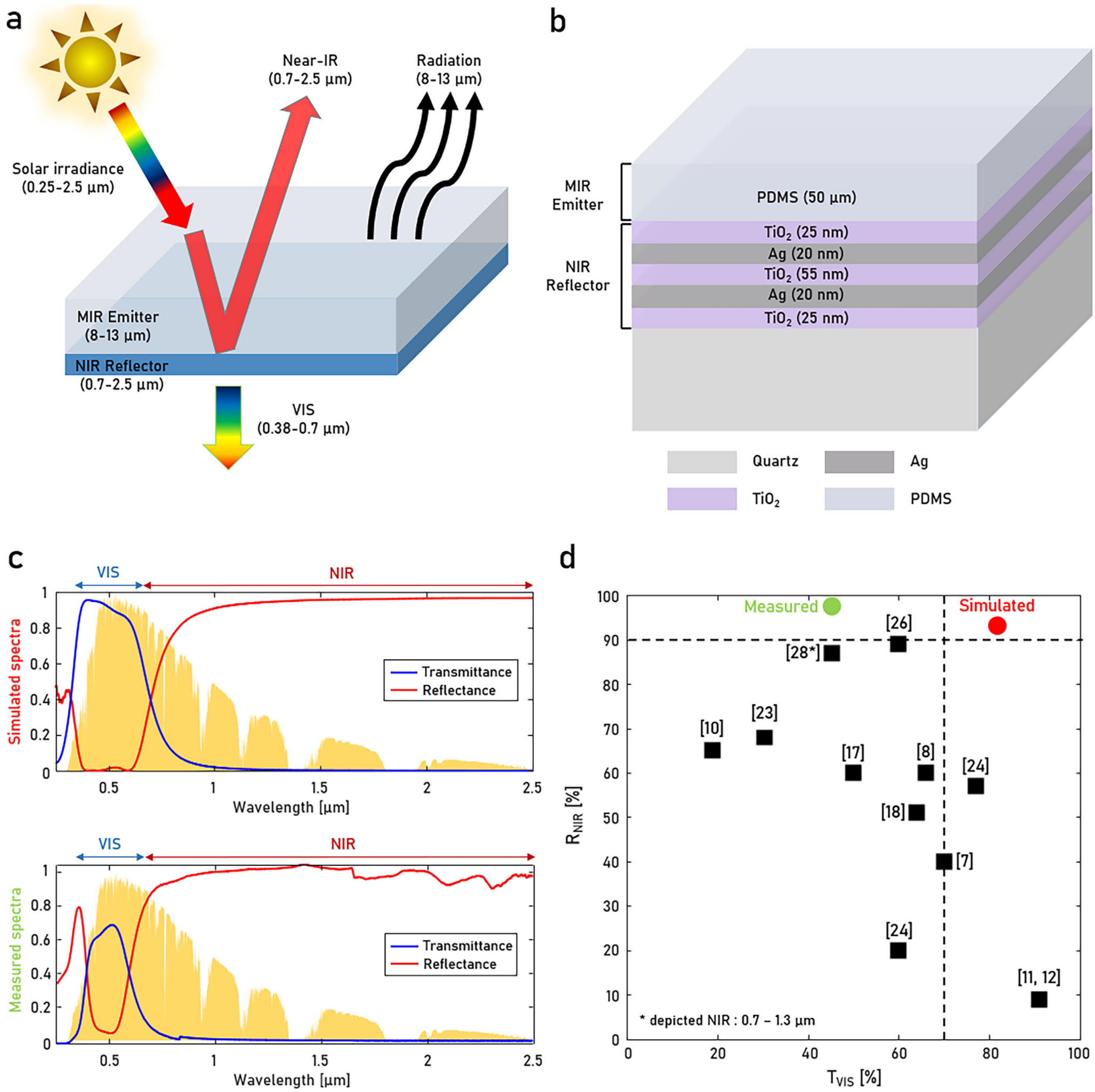

Figure 1. Concept of the transparent radiative cooler and its optical properties. a) Schematic representation of an ideal transparent radiative cooler. b) Schematic illustration of the cooler reported herein. c) Simulated and measured transmittance and reflectance spectra of the cooler. d) Comparison of the visible transparency and NIR reflectance of the cooler with those of previously reported structures. Red circles indicate the simulated data while the green circles represent the measurement data for the reported cooler.

effect has become a critical focus of recent research. To address this challenge, various materials and structural strategies such as nanoparticles,[17–19] metamaterials,[20] and multilayer designs[21–23] have been developed. In 2022, Dang et al.[24] proposed a silica grating metasurface that achieved 77% visible transmittance, 57% NIR reflectance, and a high MIR emissivity (>90%) by optimizing the optical performance across both the solar and thermal spectral regions. This structure was designed for applications such as transparent windows or glass-covered devices. In the same year, a vanadium dioxide–based smart transparent radiative cooler with a metasurface design and an aluminum-doped zinc oxide back reflector was reported.[25] This system achieved 60% visible transmittance and 20% NIR reflectance, with potential applicability in both terrestrial and space environments. In addition to metasurfaces, multilayer structures have been developed to realize sharp optical transitions at 700 nm while balancing visible transparency and NIR reflectance. Recently, a metal–dielectric multilayer structure based on silicon dioxide and silver (Ag) was reported that achieved a relatively high visible transparency (>60%), NIR reflectance (>89%), and a strong MIR emissivity (>95%).[26] Based on a sign transition of the effective permittivity at ≈700 nm, this design allowed high visible transmission while blocking solar absorption in the unwanted spectral regions to maximize the cooling effect. Another multilayer structure employing silicon dioxide, Ag, and titanium dioxide (TiO_2) to induce a similar transition at ≈700 nm demonstrated a strong spectral selectivity, achieving an average transmittance of 65% in the visible range and a reflectance of 86% in the NIR region.[27] Moreover, an all-dielectric Bragg reflector composed of hydrogenated amorphous silicon and silicon dioxide has also been proposed, which achieved 45% visible transmittance and 87% NIR reflectance.[28] This structure exhibited a sharp spectral transition at 700 nm and maintained its performance across various angles. To enable the practical application of transparent radiative coolers while maintaining a high cooling efficiency, it is essential to design structures that precisely tailor the optical properties across the visible, NIR, and MIR spectral regions.

In this paper, a visibly transparent radiative cooler based on a multilayer structure is proposed and its cooling effect is demonstrated through numerical simulations and outdoor rooftop measurements. The cooler consists of a 50 µm-thick polydimethylsiloxane (PDMS) MIR emitter and a five-layer NIR reflector with alternating dielectric–metal deposition (Figure 1b). This cooler achieves a high transmittance in the visible range (>82%) and a high reflectance in the NIR region (>92%), with the transition occurring at ≈700 nm (Figure 1c). Because of its strong spectral selectivity, this cooler also achieves both a high transparency in the visible range and strong reflection in the NIR range, satisfying an average visible transmittance of >70% and an average NIR reflectance of >90% (Figure 1d). Outdoor rooftop measurements confirm a maximum temperature reduction of 10.8 °C compared with a 50 µm-thick PDMS layer, along with a consistent cooling performance over a 24 h period. Additionally, global cooling flux simulations demonstrate the cooling effect across diverse climatic regions, supporting its practical potential for real-world implementation.

2. Results and Discussion

2.1. Spectral Transition Control and Optical Performance of the Cooler

The NIR reflector of the cooler consists of five layers stacked on a glass substrate in the following sequence: TiO_2 (25 nm), Ag (20 nm), TiO_2 (55 nm), Ag (20 nm), and TiO_2 (25 nm). In this structure, TiO_2 and Ag serve as the dielectric and metallic components, respectively, with total thicknesses of 105 and 40 nm, respectively (**Figure 2a, left)**. With a total thickness of only 145 nm, the cooler minimizes material usage and is readily compatible with thin-film deposition techniques, thereby facilitating scalable large-area fabrication. Moreover, the multilayer design does not require complex nanofabrication processes and can be prepared over large areas by sputtering and spin-coating.

While this structure is nonperiodic, to understand the origin of the sharp transition between the visible transmittance and NIR reflectance at ≈700 nm, we consider a periodic counterpart of the reflector and apply the effective medium theory (EMT).[29] The periodic counterpart is composed of five repeating pairs of TiO_2 (21 nm) and Ag (8 nm), which have the same total thickness and metal filling fraction (Figure 2a, **right)**. Its effective relative permittivity is calculated by $\epsilon_{xx} = \epsilon_{yy} = \epsilon_{\parallel} = (\epsilon_m t_m + \epsilon_d t_d)/(t_m + t_d)$ and $\epsilon_{zz} = \epsilon_{\perp} = (t_m + t_d)/(t_m/\epsilon_m + t_d/\epsilon_d)$, where subscripts $\parallel$ and $\perp$ correspond to directions parallel and perpendicular to the layers, respectively, subscripts m and d represent the metal and dielectric components, respectively, and t is the thickness.[30] While ϵ_{zz} is positive over the entire solar region, the real part of ϵ_{xx} crosses the zero ≈628 nm (Figure 2b). Across this epsilon-near-zero (ENZ) wavelength, the topology of the iso-frequency curve of the transverse magnetic (TM) mode changes from elliptical to hyperbolic (Figure 2c) following the equation:

$$\frac{{k_x}^2 + {k_y}^2}{\varepsilon_{\perp}} + \frac{{k_z}^2}{\varepsilon_{\parallel}} = \left(\frac{\omega}{c}\right)^2 \tag{1}$$

due to a sign change in the effective permittivity. In this case, k_x, k_y, and k_z represent the wavevectors in the x, y, and z directions, respectively, ω denotes the angular frequency, and c represents the speed of light in a vacuum. In the periodic counterpart, the permittivities along all x, y, and z directions remain positive below the ENZ wavelength, maintaining an ellipsoidal iso-frequency curve **(red curve**, Figure 2c). However, above the ENZ wavelength, ϵ_{zz} becomes negative, leading to a transition into a hyperbolic iso-frequency curve **(blue curve**, Figure 2c). This transition in the topology of the iso-frequency curve, which is known as the optical topological transition, is crucial for achieving wavelength-selective spectral behavior, which enables a high visible transparency and NIR reflection.[31]

Using the alternating Ag–TiO_2 multilayer configuration as the design basis, a five-layer geometry was selected for fabrication simplicity and particle swarm optimization was applied to optimize the thickness of each layer (see S1, Supporting Information for optimization details). A lab-made transfer matrix method code was used to calculate the optical response of the multilayer structure. While the transmittance and reflectance of the periodic counterpart are inverted at ≈628 nm (Figure 2d, **solid line)** and blocks the transmission of long-wavelength visible light, the current cooler undergoes the transition at a longer wavelength of 700 nm (Figure 2d, **dashed line)**.[32] This optimization allowed the cooler to maintain a higher average transmittance in the visible region (>22% higher than its hyperbolic counterpart) while effectively reflecting solar irradiance at ≈700 nm. The discrepancy between the two structures (Figure 2a) is attributed to the individual layer thickness exceeding the skin depth of Ag (12.25 nm) and TiO_2 (28.28 nm), both of which are evaluated at 700 nm. In this regime, the EMT becomes invalid, resulting in deviations in the spectral behavior. However, the precise layer design employed herein induces a sharp transition at ≈700 nm and achieves solar selectivity for transparent radiative cooling.

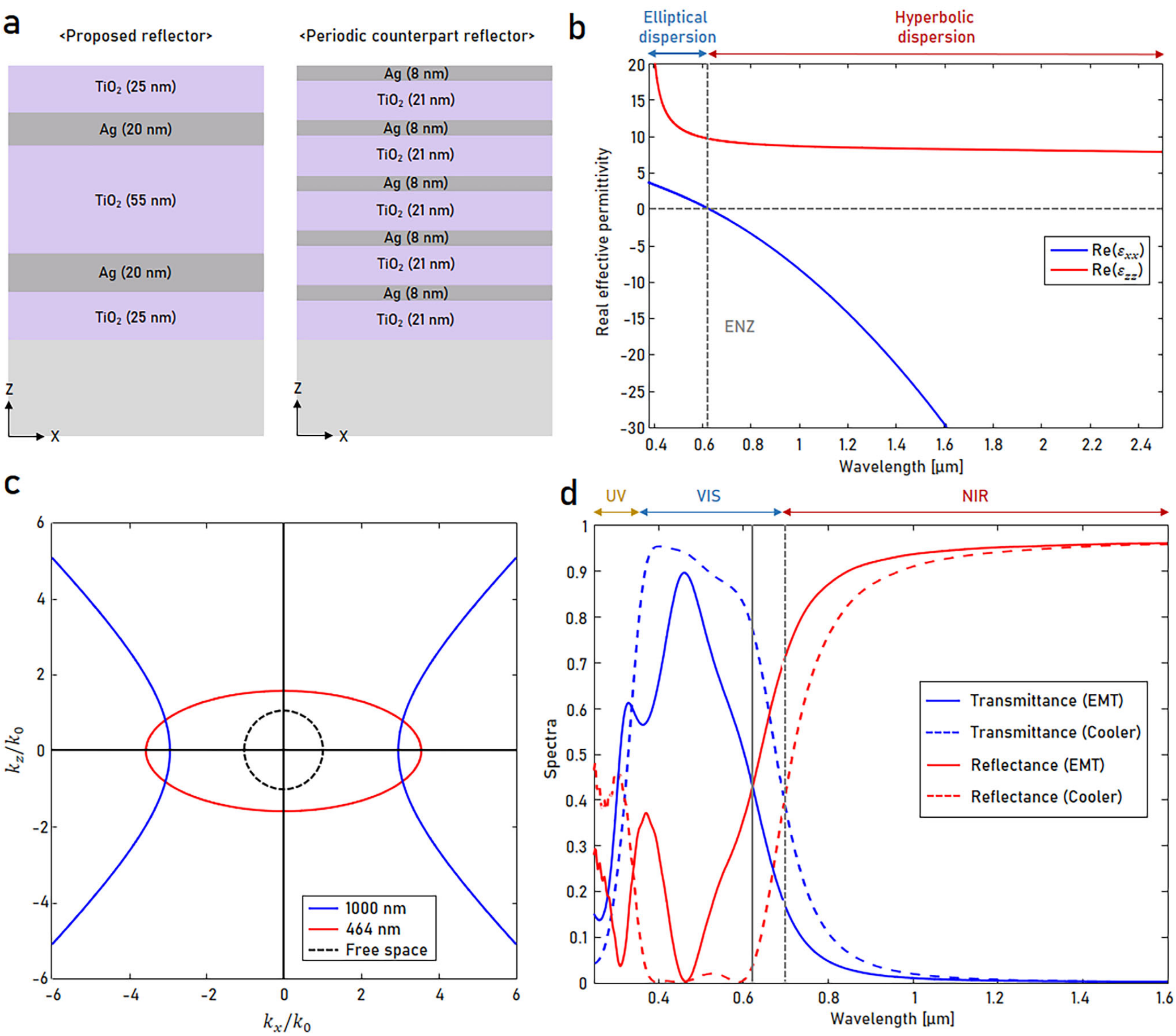

Figure 2. Optical topological transition of the NIR reflector. a) Schematic representation of the proposed reflector (left) and its periodic counterpart (right). b) Effective permittivity of the periodic counterpart, indicating the ENZ wavelength at ≈628 nm. c) Iso-frequency contours at two different wavelengths, one elliptical and the other hyperbolic. d) Simulated transmittance and reflectance spectra of the effective homogeneous slab (solid line) and the cooler (dashed line).

2.2. Optical Properties and Experimental Characteristics

The transmittance, reflectance, and absorption of the cooler in the solar and MIR regimes were measured using a UV–vis–NIR spectrophotometer and a Fourier-transform infrared spectrometer, respectively (**Figure** 3a,b). The corresponding spectra of a 50 µm-thick PDMS layer deposited on a glass substrate are also plotted for reference. The PDMS layer exhibits relatively high transmittance in the visible and NIR ranges (blue dashed curve) and low reflectance across the entire spectrum (red dashed curve). In contrast, the cooler shows a slightly lower transmittance than the PDMS layer in the visible range (blue solid) but undergoes a transition at ≈700 nm, where the reflectance increases significantly (red solid). As expected, this transition from the visible to the NIR range enables the cooler to achieve a higher reflectance at ≈700 nm.

The measured spectra show a noticeable difference from the simulated spectra, especially with respect to the transmittance. This discrepancy is attributed to slight variations in the multilayer thickness, which shift the transition wavelength and peak values and reduce the transmittance. In particular, the TiO_2 layers of the fabricated samples were observed to be thinner than designed, giving rise to an increased metal filling factor, which strengthened the metallic behavior of the NIR reflector. This mismatch reduces the visible transmittance while the NIR reflectance remains relatively robust (S2, Supporting Information). Additionally, oxidation of the Ag layers, interfacial roughness at the metal–dielectric interfaces, possible fabrication

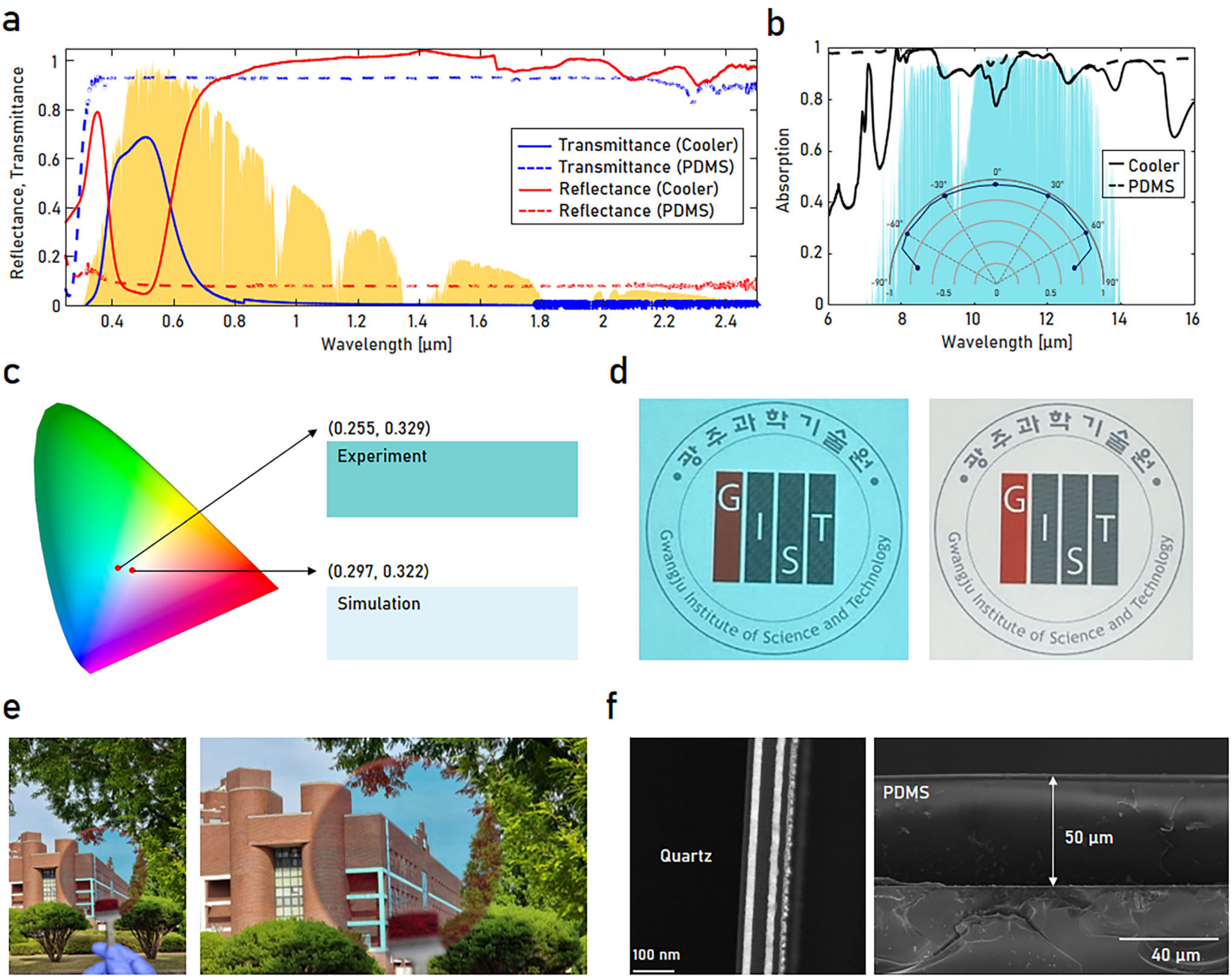

Figure 3. Optical properties and experimental characteristics of the cooler. a) Measured and simulated spectral transmittance and reflectance of the cooler and PDMS across the solar region. The yellow background represents the solar irradiance. b) Measured spectral absorption characteristics of the cooler and PDMS in the MIR region. The blue background represents the atmospheric transmittance. Inset: simulated angular absorptivity of the cooler averaged within the 8–13 µm. c) CIE 1931 xyY color space of the cooler obtained from experimental and simulated data. d) Photographic images of the cooler (left) and PDMS (right). The logo of the Gwangju Institute of Science and Technology (GIST) was used with permission, GIST, 2025. e) Photographic image demonstrating the transparency of the cooler under natural light. f) Cross-sectional TEM image confirming five-layer deposition and SEM image confirming the PDMS thickness.

imperfections (e.g., layer thickness non-uniformity or surface irregularities), and the crystal quality of the TiO_2 layer may further degrade the measured spectra. In the MIR region, the cooler exhibits emissivity similar to PDMS and the averaged absorptivity of the cooler within the atmospheric window remains high over a broad range of incident angles (Figure 3b, **inset)**. Furthermore, the cooler illustrates a stable visible transparency and NIR reflection under a wide oblique incidence up to ≈60° (see S3, Supporting Information for details regarding the angle dependence).

The color of the cooler, which was calculated from the transmittance data in both the experiments and the simulations, appears as warm white in the simulation and pale cyan in the experiments (Figure 3c). This color difference results from the aforementioned discrepancy between the simulated and measured transmittance spectra. This discrepancy is evident in the short visible wavelength region, where the measured transmittance is notably lower than the simulation, thereby giving the cooler a slightly bluish tint (Figure 3d). This suggests an effective means to tune the color of the cooler by adjusting the multilayer thickness (see S4, Supporting Information for additional details). When tested outdoors, the cooler maintained a sufficient transparency to avoid obstructing visibility (Figure 3e). This observation confirms the high potential of the cooler for practical use in real-world transparent applications, combining effective cooling with clear visibility.

Scanning electron microscopy (SEM) imaging confirmed that the PDMS layer was deposited to a thickness of 50 µm, while transmission electron microscopy (TEM) imaging verifies the successful deposition and good adhesion of the five-layered structure in the cooler (Figure 3f; see S5, Supporting Information for additional details). Notably, the layer thicknesses measured from the TEM image were 13, 19, 35, 20, and 17 nm from top to bottom, indicating that the actual Ag layers closely match the target thicknesses, whereas the TiO_2 layers exhibit deviations from the original design. More precise thickness control during fabrication will therefore be expected to enhance the visible transmittance (see Figure S1c, Supporting Information for simulated spectra based on the measured thicknesses).

2.3. Cooling Flux and Rooftop Measurements

To evaluate the cooling effect, the cooling flux (P_{cool}) of the cooler was calculated as follows:

$$P_{\mathrm{cool}}\left(T, T_{\mathrm{amb}}\right) = P_{\mathrm{rad}}\ (T) - P_{\mathrm{sun}} - P_{\mathrm{atm}}\left(T_{\mathrm{amb}}\right) - P_{cc}\left(T, T_{\mathrm{amb}}\right) \quad (2)$$

where T is the temperature of the transparent radiative cooler and T_{amb} represents the ambient temperature. Additionally, P_{sun} represents the absorbed solar radiation, P_{rad} is the thermal radiation emitted by the cooler, P_{atm} denotes the heat flux received from the atmosphere, and P_{cc} represents the conductive and convective heat transfer with the surroundings. The individual components of cooling flux can be derived as follows:

$$P_{rad} = 2\pi \iint \sin\theta \cos\theta\, I_{BB}\,(T, \lambda)\ \varepsilon\,(\lambda, \theta)\ d\lambda\ d\theta \quad (3)$$

$$P_{atm} = 2\pi \iint \sin\theta \cos\theta\, I_{BB}\left(T_{amb}, \lambda\right)\ \varepsilon_{amb}\,(\lambda, \theta)\, \varepsilon\,(\lambda, \theta)\ d\lambda\ d\theta \quad (4)$$

$$P_{sun} = \int I_{AM}\,(\lambda)\ \varepsilon\left(\lambda, \theta_{sun}\right)\ d\lambda \quad (5)$$

$$P_{cc} = h_{cc}\left(T_{amb} - T\right) \quad (6)$$

where θ represents the incident angle, ϵ and ϵ_{amb} indicate the emissivity of the radiative cooler and the ambient emissivity, respectively, I_{BB} is the spectral irradiance of a blackbody, I_{AM} indicates the intensity of solar radiation, and h_{cc} is the conduction and convection coefficient. According to Equation (2), maximizing the cooling effect requires enhancing absorption in the atmospheric window to maximize P_{rad}, while simultaneously minimizing P_{sun} by reflecting solar irradiance in all regions except the visible spectrum.

To compute the cooling flux, each parameter (P_{rad}, P_{sun}, P_{atm}, and P_{cc}) of the cooler was evaluated and compared with that of PDMS (**Figure 4a**). The calculations were based on the measured data from Figure 3a and were performed using ViBA Rad[33] with fixed conditions of $T = 303$ K and $h_{\mathrm{cc}} = 6$ $\mathrm{Wm^{-2}\ K^{-1}}$. Figure 4a shows that P_{rad} and P_{atm}, which include the emissivity term ϵ, are slightly higher for PDMS due to their slightly higher absorption characteristics. However, a significant difference was observed for P_{sun}, since the cooler effectively reflected solar irradiance in the NIR range. As a result, the cooler exhibited a considerably lower P_{sun} than PDMS. By incorporating these parameters into the P_{cool} calculation, it was deduced that the cooler outperforms PDMS by ≈548 $\mathrm{Wm^{-2}}$ (Figure 4b). This result highlights that compared with the bare PDMS, the cooler reduces P_{sun} from 780 to 399 $\mathrm{Wm^{-2}}$ and thus leads to a significantly higher cooling effect overall. To validate the radiative cooling performance under real-world conditions, rooftop measurements were conducted using a setup consisting of nested acrylic boxes mounted on a wooden frame (Figure 4c). Each box contained either the cooler, PDMS, or was left empty (Figure 4d). The ambient temperature was recorded using a thermometer placed inside an identical acrylic box without any film. The overall experimental setup and outdoor environment are shown in Figure 4e. Continuous temperature measurements were conducted from 19:40 on 26 June 2024 to 19:40 on 28 June 2024 (see S6, Supporting Information for detailed measurements). The cooler consistently exhibited a lower surface temperature (T_{RC}) compared with that of PDMS (T_{PDMS}) (Figure 4f). Notably, the temperature within the inner acrylic box enclosing the cooler remained remarkably close to the ambient temperature throughout the measurement period, despite the air-isolated configuration, due to radiative cooling **(blue and cyan curves**, Figure 4f). It was also observed that the temperature difference ($\Delta T = T_{\mathrm{PDMS}} - T_{\mathrm{RC}}$) between the cooler and PDMS increased under solar irradiance (Figure 4g). Furthermore, T_{RC} remained consistently lower than T_{PDMS}, even throughout the night, indicating effective nighttime radiative cooling. Specifically, on 27th June, the average temperature difference between PDMS and the cooler was 4.42 °C between 07:00 and 19:40, and 6.21 °C between 10:00 and 15:00, with a maximum difference of 6.9 °C observed at 11:44. On 28th June, the average temperature difference was 5.98 °C between 07:00 and 19:40, and 8.56 °C between 10:00 and 15:00, reaching a maximum of 10.8 °C at 13:34.

The cooling performance of a vertically oriented cooler was also evaluated to assess the practical applicability of the cooler to real building surfaces. Despite a reduced degree of solar reflection, the film achieved 2 °C sub-ambient cooling and outperformed PDMS by up to 2.9 °C (see S7, Supporting Information for additional details).

2.4. Global Cooling Flux

As the cooling performance varies significantly depending on the local climate and weather, the spatially varying Earth skin temperature and solar irradiance across the world were considered to evaluate the global potential of the developed radiative cooler. A global map of the cooling flux difference (ΔP_{cool}) between the cooler and PDMS is presented in **Figure 5a**. This simulation employed Earth skin temperature and solar irradiance data for the month of July, which was obtained from the NASA Langley Research Center (LaRC) POWER Project.[34] Using a lab-made code based on Equations (3)–(6) along with the measured data from Figure 3, the cooling flux was calculated at each terrestrial point, assuming that the cooler was positioned in an absorbing chamber. The results indicate a widespread cooling potential, with better cooling performance being predicted compared with that of PDMS across most regions (S8, Supporting Information).

Finally, the cooling flux of the cooler was examined for six selected cities, namely Los Angeles (LA), Berlin, Cairo, New Delhi, Beijing, and Seoul. The cooler exhibited a positive cooling flux across all six cities (Figure 5b), reaching a maximum of 85.9

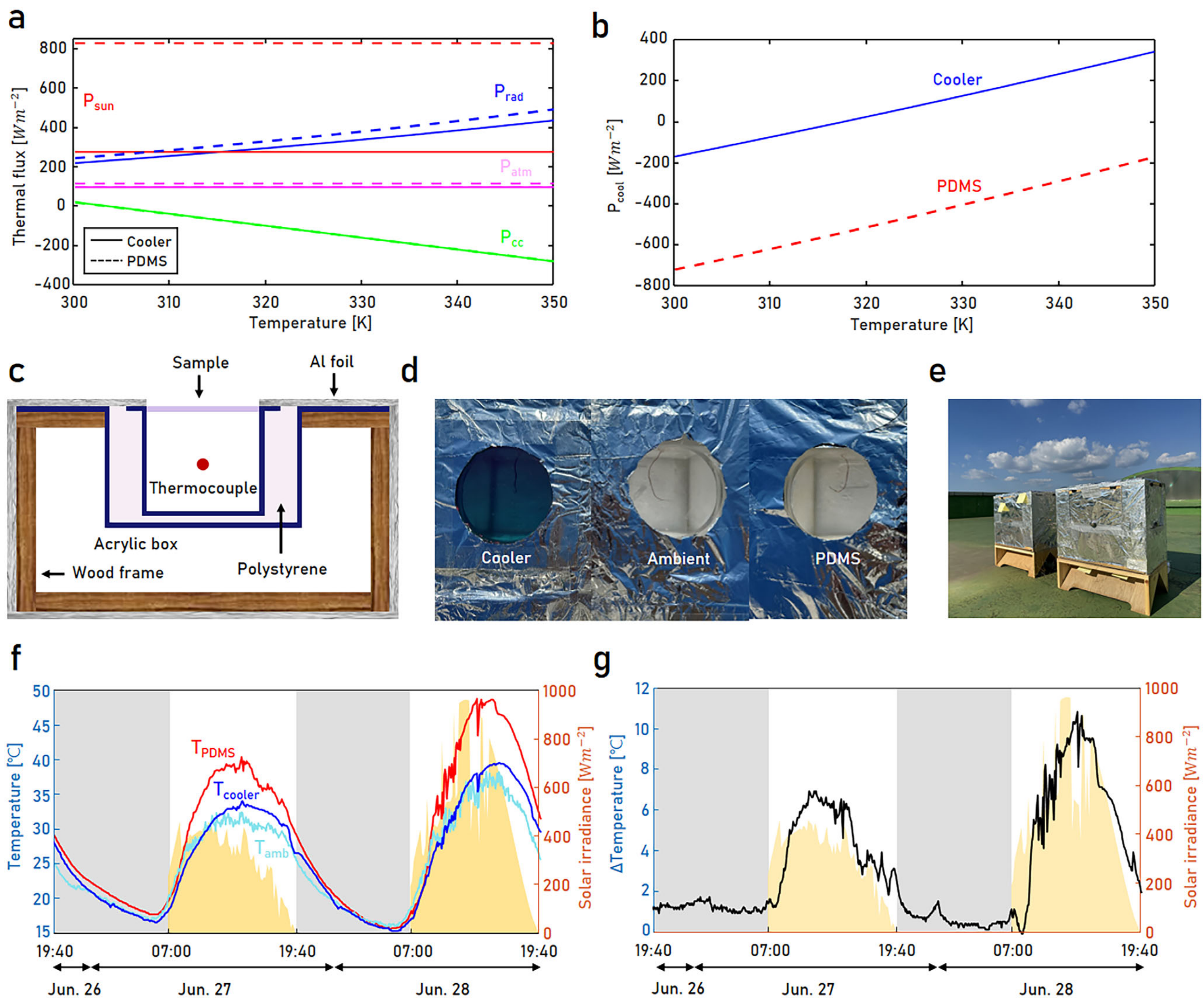

Figure 4. Cooling flux analysis and rooftop measurements performed for the cooler. a) Cooling flux components (P_{rad}, P_{atm}, P_{sun}, and P_{cc}) and b) total cooling flux (P_{cool}) of the cooler and PDMS computed from the measured spectra. c–g) Results of rooftop measurements conducted at Yonsei University, Wonju, Republic of Korea, from 19:40 on 26 June 2024 to 19:40 on 28 June 2024. (c) Photographic image of the experimental setup for the rooftop measurements. (d) Close-up view of the individual acrylic boxes for ambient temperature monitoring, one of which is empty. The other boxes contain either the cooler or PDMS. (e) Overview of the rooftop outdoor experimental environment. (f) Time-resolved temperatures of the cooler and PDMS. The yellow background indicates the measured solar irradiance. (g) Temperature difference (ΔT) between the cooler and PDMS.

Wm^{-2} in New Delhi and a minimum of 55.2 Wm^{-2} in Cairo. In contrast, the cooling flux of PDMS was negative across all six cities, ranging from a maximum of −30.1 Wm^{-2} in Seoul to a minimum of −132.4 Wm^{-2} in Cairo. Notably, ΔP_{cool} shown in Figure 5c remains positive in each of the six cities. The distribution of the cooling flux difference exhibited a strong correlation with solar irradiance (Figure 5d). This was further supported by the similarity in their spatial distributions (Figure 5a; Figure S7b, Supporting Information). These results demonstrate the global potential of the cooler, which effectively blocks solar radiation in the NIR range to substantially reduce heat absorption, thereby allowing efficient heat emission in the MIR range and achieving a strong cooling effect.

3. Conclusion

In this study, a visibly transparent radiative cooler was proposed and developed using a multilayer structure consisting of a PDMS emitter and a TiO_2-Ag-based NIR reflector. The sharp transition between a high visible transmittance and NIR reflectance at ≈700 nm was discussed using the topological transition of the iso-frequency curve of the periodic counterpart from a closed to an open shape. The thickness of each layer was optimized to enhance both the visible transmittance and the NIR reflectance, thereby achieving better visible transparency than its counterpart. The fabricated cooler demonstrated a maximum temperature reduction of 10.8 °C in outdoor rooftop measurements and

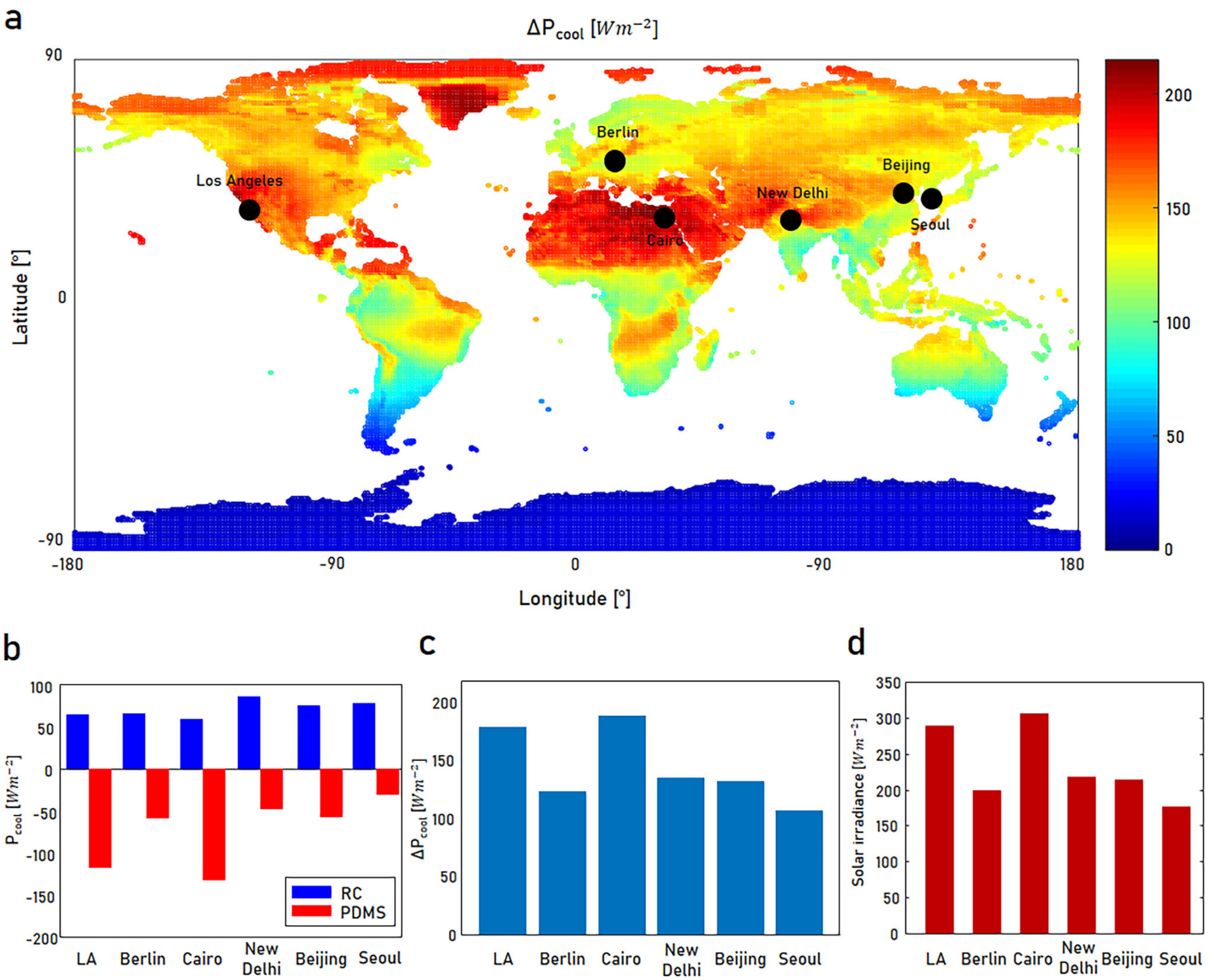

Figure 5. Evaluation of the global radiative cooling potential. a) Difference between the cooling flux of the cooler and PDMS (ΔP_{cool}) represented on a worldwide map. b) Cooling flux (P_{cool}) of the cooler and PDMS. c) Cooling flux difference between the cooler and PDMS. d) Solar irradiance in six selected cities.

showed a robust cooling performance across different climates in global cooling simulations. These findings highlight the practical feasibility of the developed cooler for energy-saving applications in buildings, electronics, and other transparent surface-integrated systems.

4. Experimental Section

Sample Fabrication: The cooler was fabricated using magnetron reactive sputtering. TiO_2 was deposited via reactive sputtering by introducing O_2 gas to a Ti target, while Ag was deposited using magnetron sputtering on a 4-inch quartz glass substrate. After deposition, PDMS was applied by spin coating, wherein a 10:1 mixture of PDMS and a curing agent were spun at 1350 rpm for 60 s. The coated sample was cured on a hot plate at 70 °C for 3 h. The PDMS sample was subjected to the same spin-coating and curing process.

Measurement of the Optical Properties: To analyze the optical properties of the sample in the solar range, the transmittance and reflectance were measured in the 0.25–2.5 µm range using a UV–vis–NIR spectrophotometer (LAMBDA 950, Perkin Elmer) equipped with an integrating sphere. For the MIR range, the absorptivity was obtained in the 6–16 µm range by measuring the transmittance and reflectance using Fourier-transform infrared spectrometry (Vertex 70v, Bruker). SEM (Verios 5 UC, Thermo Fisher Scientific) was employed to capture the side view of the PDMS layer, while TEM (Talos F200X G2, Thermo Fisher Scientific) was used to image the side view of the five-layered structure in the reflector.

Rooftop Measurements: A rooftop measurement was conducted to evaluate the cooling capabilities of the 4-inch wafer-sized cooler and PDMS under ambient conditions. The experimental setup was designed to minimize extraneous heat transfer and isolate the radiative cooling effect.

The central component of the apparatus consisted of a multilayered chamber. An outer supporting frame, constructed of wood and measuring 50 cm in length, 30 cm in width, and 40 cm in height, was clad in aluminum foil to mitigate solar heating by reflecting incident radiation. Within this frame, a dual-chamber configuration was implemented using concentric acrylic boxes. The interstitial space between these boxes was filled with expanded polystyrene (PS), which was selected for its exceptional thermal insulation properties. This PS layer served as a critical barrier against conductive heat transfer from the surrounding environment. By surrounding the inner acrylic chamber with PS and ensuring the samples had no direct contact with the PS, thermal exchange through conduction was minimized, thereby isolating radiative heat exchange. This design ensured that temperature variations within the inner chamber (7 cm high, 9 cm × 9 cm wide) were predominantly driven by radiative heat transfer.

The 4-inch cooler and PDMS samples were each affixed as windows to individual inner acrylic chambers, creating sealed enclosures that isolated each chamber from the ambient environment. This arrangement permitted direct exposure of the samples to the sky, facilitating radiative heat loss while preventing convective air exchange with the external environment.

Temperature measurements were conducted using K-type thermocouples positioned at the geometric center of each sealed inner chamber. To establish a baseline, the temperature inside an identical acrylic box without any film was measured using a K-type thermocouple. Temperature data were continuously logged at 5 min intervals using a data logger (HH520, OMEGA Engineering). This temporal resolution allowed detailed analysis of the temperature fluctuations and the dynamic cooling responses of the samples.

The solar irradiance data, which were crucial for evaluating the influence of solar radiation, were obtained from satellite measurements provided by the Korea Institute of Energy Research. Global Horizontal Irradiance (GHI) data was employed to represent the total amount of solar radiation received on a horizontal surface.

Supporting Information

Supporting Information is available from the Wiley Online Library or from the author.

Acknowledgements

J.B. and M.J. contributed equally to this work. This work was financially supported by National Research Foundation grants (RS-2023-00218908, RS-2025-00556856) funded by the Ministry of Science and ICT of the Korean government.

Conflict of Interest

The authors declare no conflict of interest.

Data Availability Statement

The data that support the findings of this study are available from the corresponding author upon reasonable request.

Keywords

daytime radiative cooling, rooftop measurement, selective reflector, thermal emission, transparency

Received: May 12, 2025
Revised: August 25, 2025
Published online: September 8, 2025

[1] Z. Li, Q. Chen, Y. Song, B. Zhu, J. Zhu, *Adv. Mater. Technol.* **2020**, *5*, 1901007.
[2] S. So, J. Yun, B. Ko, D. Lee, M. Kim, J. Noh, C. Park, J. Park, J. Rho, *Adv. Sci.* **2024**, *11*, 2305067.
[3] C. G. Granqvist, A. Hjortsberg, *J. Appl. Phys.* **1981**, *52*, 4205.
[4] Z. Yan, H. Zhai, D. Fan, Q. Li, *Prog. Mater. Sci.* **2024**, *144*, 101291.
[5] M. Li, Z. Yan, D. Fan, *ACS Appl. Mater. Interfaces* **2023**, *15*, 17848.
[6] C. Lin, K. Li, M. Li, B. Dopphoopha, J. Zheng, J. Wang, S. Du, Y. Li, B. Huang, *Adv. Mater.* **2025**, *37*, 2409738.
[7] Y. Li, X. Chen, L. Yu, D. Pang, H. Yan, M. Chen, *ACS Appl. Mater. Interfaces* **2023**, *15*, 4122.
[8] H. Zou, C. Wang, J. Yu, D. Huang, R. Yang, R. Wang, *Cell Rep. Phys. Sci.* **2023**, *4*, 101539.
[9] Z. Yi, D. Xu, J. Xu, H. Qian, D. Zhao, R. Yang, *Energy Built Environ.* **2021**, *2*, 214.
[10] B. Zhao, C. Wang, M. Hu, X. Ao, J. Liu, Q. Xuan, G. Pei, *Energy* **2022**, *238*, 121761.
[11] K. W. Lee, W. Lim, M. S. Jeon, H. Jang, J. Hwang, C. H. Lee, D. R. Kim, *Adv. Funct. Mater.* **2022**, *32*, 2105882.
[12] Y.-H. Chen, C.-W. Hwang, S.-W. Chang, M.-T. Tsai, K. N. Jayakumaran, L.-C. Yang, Y.-C. Lo, F.-H. Ko, H.-C. Wang, H.-L. Chen, D. Wan, *Adv. Funct. Mater.* **2023**, *33*, 2301924.
[13] G. Zhu, Z. Yan, W. Yao, H. Zhai, Q. Li, D. Fan, *Chem. Eng. J.* **2025**, *518*, 164568.
[14] J. Huang, M. Li, D. Fan, *Appl. Mater. Today* **2021**, *25*, 101209.
[15] T. Li, Y. Zhai, S. He, W. Gan, Z. Wei, M. Heidarinejad, D. Dalgo, R. Mi, X. Zhao, J. Song, J. Dai, C. Chen, A. Aili, A. Vellore, A. Martini, R. Yang, J. Srebric, X. Yin, L. Hu, *Science* **2019**, *364*, 760.
[16] A. P. Raman, M. A. Anoma, L. Zhu, E. Rephaeli, S. Fan, *Nature* **2014**, *515*, 540.
[17] M.-Q. Lei, Y.-F. Hu, Y.-N. Song, Y. Li, Y. Deng, K. Liu, L. Xie, J.-H. Tang, D.-L. Han, J. Lei, Z.-M. Li, *Opt. Mater.* **2021**, *122*, 111651.
[18] Y. Xu, Y. Fang, S. Tao, Z. Fang, Y. Ni, C. Lu, C. Xu, W. Li, Z. Xu, *Compos. Commun.* **2023**, *43*, 101717.
[19] Z. Yan, G. Zhu, D. Fan, Q. Li, *Adv. Funct. Mater.* **2025**, *35*, 2412261.
[20] B. Ko, J. Noh, D. Chae, C. Lee, H. Lim, H. Lee, J. Rho, *Adv. Funct. Mater.* **2024**, *34*, 2410613.
[21] Z. Zhou, X. Wang, Y. Ma, B. Hu, J. Zhou, *Cell Rep. Phys. Sci.* **2020**, *1*, 100231.
[22] Y. Zhu, H. Luo, C. Yang, B. Qin, P. Ghosh, S. Kaur, W. Shen, M. Qiu, P. Belov, Q. Li, *Light Sci. Appl.* **2022**, *11*, 122.
[23] S. Kim, W. Shang, S. Moon, T. Pastega, E. Lee, T. Luo, *ACS Energy Lett.* **2022**, *7*, 4134.
[24] S. Dang, X. Wang, H. Ye, *Adv. Mater. Interfaces* **2022**, *9*, 2201050.
[25] K. Sun, W. Xiao, C. Wheeler, M. Simeoni, A. Urbani, M. Gaspari, S. Mengali, C. H. (K.) de Groot, O. L. Muskens, *Nanophotonics* **2022**, *11*, 4101.
[26] Y. Jin, Y. Jeong, K. Yu, *Adv. Funct. Mater.* **2023**, *33*, 2207940.
[27] H. Nan, P. Xiong, G.-J. Zhong, Y. Li, R. Li, J.-H. Niu, J. Lei, Z.-M. Li, *ACS Appl. Nano Mater.* **2024**, *7*, 17111.
[28] M. Kim, D. Lee, S. Son, Y. Yang, H. Lee, J. Rho, *Adv. Opt. Mater.* **2021**, *9*, 2002226.
[29] C. L. Cortes, W. Newman, S. Molesky, Z. Jacob, *J. Opt.* **2012**, *14*, 063001.
[30] B. Wood, J. B. Pendry, D. P. Tsai, *Phys. Rev. B* **2006**, *74*, 115116.
[31] H. N. S. Krishnamoorthy, Z. Jacob, E. Narimanov, I. Kretzschmar, V. M. Menon, *Science* **2012**, *336*, 205.
[32] J. Kennedy, R. Eberhart, in *Proceedings of ICNN'95-International Conference on Neural Networks*, IEEE **1995**, pp. 1942–1948.
[33] D. Lee, S. Kwon, M. Kim, *SoftwareX* **2023**, *24*, 101562.
[34] NASA Langley Research Center (LaRC) POWER project, https://power.larc.nasa.gov/data-access-viewer/ (accessed: December **2020**).